

Optical Engineering

OpticalEngineering.SPIEDigitalLibrary.org

Polarization effects associated with thermal processing of HY-80 structural steel using high-power laser diode array

Sheldon S. Q. Wu
Bradford W. Baker
Mark D. Rotter
Alexander M. Rubenchik
Maxwell E. Wiechec
Zachary M. Brown
Raymond J. Beach
Manyalibo J. Matthews

SPIE.

Sheldon S. Q. Wu, Bradford W. Baker, Mark D. Rotter, Alexander M. Rubenchik, Maxwell E. Wiechec, Zachary M. Brown, Raymond J. Beach, Manyalibo J. Matthews, "Polarization effects associated with thermal processing of HY-80 structural steel using high-power laser diode array," *Opt. Eng.* **56**(12), 124108 (2017), doi: 10.1117/1.OE.56.12.124108.

Polarization effects associated with thermal processing of HY-80 structural steel using high-power laser diode array

Sheldon S. Q. Wu,^{a,*} Bradford W. Baker,^b Mark D. Rotter,^a Alexander M. Rubenchik,^a Maxwell E. Wiechec,^b Zachary M. Brown,^b Raymond J. Beach,^a and Manyalibo J. Matthews^{a,*}

^aLawrence Livermore National Laboratory, Livermore, California, United States

^bUnited States Naval Academy, Annapolis, Maryland, United States

Abstract. Localized heating of roughened steel surfaces using highly divergent laser light emitted from high-power laser diode arrays was experimentally demonstrated and compared with theoretical predictions. Polarization dependence was analyzed using Fresnel coefficients to understand the laser-induced temperature rise of HY-80 steel plates under 383- to 612-W laser irradiation. Laser-induced, transient temperature distributions were directly measured using bulk thermocouple probes and thermal imaging. Finite-element analysis yielded quantitative assessment of energy deposition and heat transport in HY-80 steel using absorptivity as a tuning parameter. The extracted absorptivity values ranged from 0.62 to 0.75 for S-polarized and 0.63 to 0.85 for P-polarized light, in agreement with partially oxidized iron surfaces. Microstructural analysis using electron backscatter diffraction revealed a heat affected zone for the highest temperature conditions (612 W, P-polarized) as evidence of rapid quenching and an austenite to martensite transformation. The efficient use of diode arrays for laser-assisted advanced manufacturing technologies, such as hybrid friction stir welding, is discussed. © 2017 Society of Photo-Optical Instrumentation Engineers (SPIE) [DOI: 10.1117/1.OE.56.12.124108]

Keywords: diode lasers; laser materials modification; thermal effects.

Paper 171250 received Aug. 8, 2017; accepted for publication Nov. 28, 2017; published online Dec. 23, 2017.

1 Introduction

Since the advent of efficient, low cost, and high average power laser diodes, optical pumping of solid-state lasers has been greatly advanced, producing unprecedented output power and thermal control of high-power laser systems.¹⁻³ Beyond diode-pumped solid-state lasers (DPSSL), such as fiber and disc lasers, efficient pumping of alkali vapor lasers⁴ has enabled compact, high Strehl ratio multikilowatt class continuous lasers important in industrial and defense applications. However, direct use of diode laser sources in laser materials processing has been limited due to the poor mode quality, broad spectral, and low coherent properties of laser diode arrays typically used in diode pumping schemes relative to DPSS or gas laser systems. The requirement for tight focusing and high irradiance, which demands high mode quality ($M^2 \sim 1$), is usually the driving factor in choice of laser sources for laser-based microprocessing of materials.⁵ For example, to raise the temperature of a refractory metal above the melt point while traversing at rates of ~ 1 m/s requires an irradiance to beam radius product of $I \times a \sim 10$ MW $\mu\text{m}/\text{cm}^2$.⁶ However, in applications where relevant length scales are larger and submelting point temperatures are required, these requirements are relaxed while laser/heat source efficiency and cost become more important. Examples of these lower irradiance, high efficiency applications are laser sintering,⁷ laser polishing,⁸ and laser-assisted friction stir welding (LAFSW).^{9,10} In these applications, >1 mm scale irradiation is preferred and temperatures between softening and melting are required.

In the case of LAFSW, typical stir weld tool sizes range from 0.5 to 2 in. implying that laser used to assist in the process be commensurate and need not focus tightly as in the case for welding, cutting, etc. One of the earliest demonstrations of LAFSW was provided by Kohn et al.,¹⁰ who used a 700-W Nd:YAG laser to join two magnesium alloy plates in a butt weld configuration. In this early demonstration, the efficacy of a using a comparatively small laser system to preheat a very small area ahead of the friction stir welding (FSW) tool (1 cm diameter) to $\sim 320^\circ\text{C}$ without detrimental effect to the base workpiece was shown. Since that early demonstration, different LAFSW setups have been used on aluminum and magnesium alloys in traditional butt weld configurations¹¹⁻¹⁴ and lap weld configurations,¹⁵ as well as nickel-based alloys,¹⁶ and steels^{17,18} although the total number of LAFSW demonstrations remains limited. Campanelli and Casalino¹¹⁻¹³ evaluated the changes in aluminum alloy microstructure, microhardness, residual stress, and tensile properties following LAFSW under typical FSW conditions and using a 4 kW ytterbium fiber laser and concluded that LAFSW was capable of improving material conditions of the weld nugget. Adding to the complexity of temperature control during LAFSW, Sun et al.^{17,18} developed a LAFSW setup that used a YAG laser with a conventional FSW machine and observed the formation of a brittle martensite phase within a carbon steel workpiece that could be prevented by judicious selection of welding parameters, most notably tool traverse speed, in order to control the cooling rate following welding. The formation of martensite in carbon steels during rapid cooling from elevated temperatures requires additional control of temperature during preheating,

*Address all correspondence to: Sheldon S. Q. Wu, E-mail: wu31@llnl.gov; Manyalibo J. Matthews, E-mail: matthews11@llnl.gov

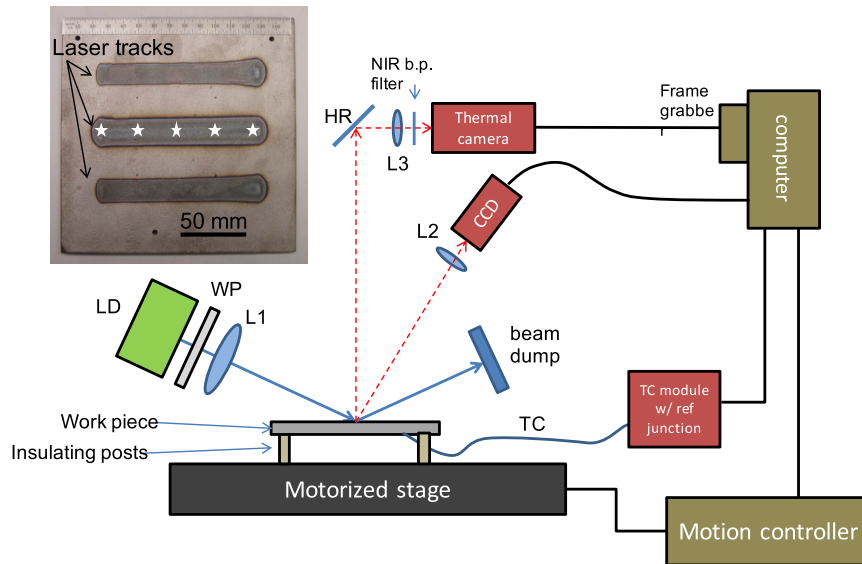


Fig. 1 High-power laser diode test bed. LD, 794-nm laser diode array; WP, halfwave plate; L1, $f/3$ cylindrical lens; L2, $f/8$ camera lens; L3 $f/4$ camera lens; TC, thermocouple wires. Inset shows an image of a bead-blasted HY-80 steel plate following three laser exposures where the stars identify the locations of the embedded thermocouples.

welding, and postweld cooling that does not exist in other alloy systems. This complexity prevents the indiscriminate heating of steels to high temperatures solely to reduce frictional forces during FSW.

Because of the inherent nonuniform irradiation pattern resulting from arrays of diodes, it is important to understand the relationship between diode irradiance in practice and laser-induced temperature in metal substrates. Furthermore, because mechanical tooling often impinges at a normal angle to the part surfaces, off-axis illumination must be used in a laser-assisted configuration, and therefore, the polarization of the light can play an important role in optimizing energy coupling. In this work, we analyze the temperature rise in HY-80 steel test plates caused by laser irradiation at a high angle of incidence and compare our results to finite-element modeling of laser-induced heating. It is well-known that surface roughness, oxidation, defects, etc., can affect optical absorption and therefore cause difficulty in a priori determination of its value. Using absorptivity as a single fit parameter, we generate a transient thermal model using measurements from embedded thermocouples and predict surface temperature variations due to laser scanning. Microstructural changes within the heat-affected zone (HAZ) below the surface were evaluated using optical microscopy, electron microscopy, and electron backscatter diffraction (EBSD) and indicate the creation of a quenched martensite phase from a high-temperature austenite phase. A $\sim 25\%$ decrease in absorptivity was determined for S-polarized light compared to P-polarized, consistent with an observed decrease in HAZ, which was less than predicted for either iron or iron oxide (Fe_3O_4) at 60-deg angle of incidence based on the Fresnel equations. The effect of polarization-dependent absorptivity has not been widely investigated in the context of laser heating and represents a significant gap in knowledge considering that most laser systems produce polarized or partially polarized light. The efficacy of laser-assisted material processing using off-axis, high power diode lasers is discussed.

2 Experimental Setup

The laser diode test setup is shown in Fig. 1. The laser diode source (Northrup Grumman) consists of a 60-bar continuous wave diode array operating at ~ 793 nm (2.6-nm FWHM), with a maximum output power of 5.1 kW and slope efficiency per bar of 1.1 W/A. The divergence of the laser source is 2.6 and 81.1 mrad along the fast and slow axis, respectively, and oriented such that the slow axis is perpendicular to the plane of incidence. Laser light emerges S-polarized relative to the plate surface and can be rotated with a quartz halfwave-plate to P-polarization. After passing the wave-plate position, light is focused using a 200-mm focal length cylindrical lens. The laser spot size at the sample is nominally 0.5×1 cm with the short axis along the P direction. Samples consisted of $6.35 \times 152.4 \times 152.4$ mm³ plates of HY-80 steel, which were either bead- or grit-blasted prior to laser irradiation.

Thermal radiation from the sample surface is imaged using an InGaAs camera (320×256 pixel, Sensors Unlimited) equipped with a 1535 ± 41 nm narrow bandpass filter and a 50-mm 1:1.4 camera lens. The resolution on the camera chip is $170 \mu\text{m}/\text{pixel}$. The thermal emission count is calibrated using a standard blackbody source up to 1200°C ¹⁹ and an emissivity value of 0.4. Direct temperature measurements were also made using a series of embedded thermocouples placed along the scan path at 1 in. (25.4 mm) intervals at depths from the irradiated surface ranging from 0.6 to 5.7 mm. Final calibration of the IR imaging system was performed using the thermocouple data and simulated peak temperature values for each experiment.

For the microstructural analysis, samples were prepared with SiC papers and diamond polishing solutions. Samples for microscopy were etched with 2% NITAL and were analyzed in an optical microscope and a field emission gun scanning electron microscope at 15 keV. Energy dispersive x-ray spectroscopy (EDS) was also performed on the base material and HAZ to determine if any change in composition of

an element in a particular area. Specimens for EBSD were polished to a final step of 0.05- μm colloidal silica on a vibratory polisher and were analyzed unetched using a TESCAN MIRA3 field emission gun electron microscope at 20 keV with a step size of 0.1 mm.

3 Finite-Element Analysis of Nonuniform, Off-Axis Laser Heating

3.1 Optical and Physical Properties of HY-80 Steel

In complementary laser heating for FSW or other tooling applications, it is desirable to deliver the energy very close to the work piece to limit irradiance loss from beam divergence. On the other hand, it is beneficial to implement the auxiliary heating in such a way to maximize compatibility with existent FSW systems. We suggest an illumination scheme, which addresses both concerns, namely to direct laser light at an oblique angle relative to the processed plate (Fig. 1). In this case, the heating system can deliver the energy close to the workpiece and will not interfere

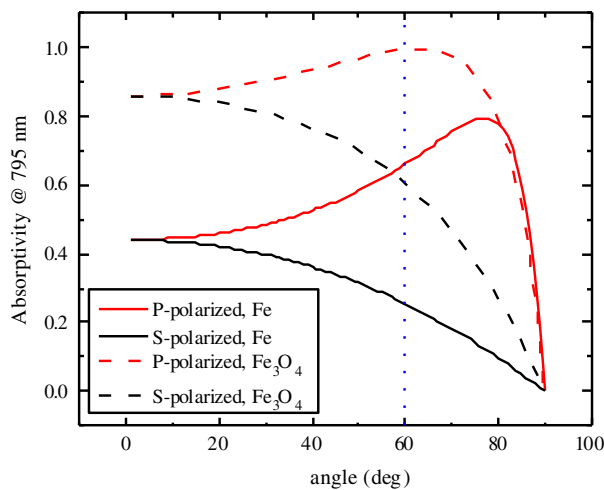


Fig. 2 Calculated Fresnel absorptivity curves as a function of incidence angle and polarization for wrought iron (solid curves) and iron oxide, Fe_3O_4 (dashed curves) at an operating wavelength of 795 nm. The dotted vertical line indicates the angle of incidence used in the setup (60 deg).

with existent welding arrangement. The diode radiation is highly polarized, and we can arrange the incident light to be P-polarized thus enhancing the energy coupling.

The angular dependence of S- and P-polarized light for unoxidized wrought iron surfaces (close approximation to low carbon steel) is presented in Fig. 2 as a pair of solid curves. The wrought iron absorptivity was derived using the Fresnel equations and optical constants $n = 2.91$ and $k = 3.34$ at 795 nm.²⁰ As shown in Fig. 2, a large difference between S- and P-polarized light occurs for angles greater than ~ 20 deg and is close to 24% and 63%, respectively, at an incidence angle of 60 deg, where we have tuned our system. Because the HY-80 plates were exposed to air prior and during processing, we also show, in Fig. 2, the S- and P-polarized absorptivity curves (dashed curves) for an iron oxide film (magnetite, Fe_3O_4), using optical constants $n = 2.16$ and $k = 0.29$ at 795 nm²¹ and based on a film thickness of ~ 40 nm. As shown, the presence of an oxide layer leads to an increase in absorptivity at both polarizations, with S-polarized light absorptivity near 60% and P-polarized absorptivity near 99%. Calculations were done for an ideal flat surface.

In practice, the surface waviness from machining, handling defects, and nonuniform roughness can greatly affect the absorptivity for such oblique light incidence.²² With limited knowledge about specific surface roughness parameters for our test plates, as well as for typical parts used in realistic FSW applications, one should defer to empirical observations. To prepare the sample surfaces, we grit or bead blasted the samples to produce clean and uniform roughness surfaces. The typical final sample appearance of a grit- and bead-blasted sample is presented in Fig. 3. We see from Figs. 3(a) and 3(c) a variation of the surface on the scale much longer than the light wavelength. Surface morphology variations are visible for the bead-blasted case, Figs. 3(b) and 3(d), due to minor ~ 100 - μm indentations from the beads, which contrasted the finer scale features on the grit-blasted samples. We also note that the bead-blasted surfaces appeared somewhat shinier compared to grit-blasted surfaces, and over time (several days following the experiments) shows signs of rust more readily. The surface height variations imply that locally the orientation of the incident light's polarization with respect to the plane of incidence and the corresponding

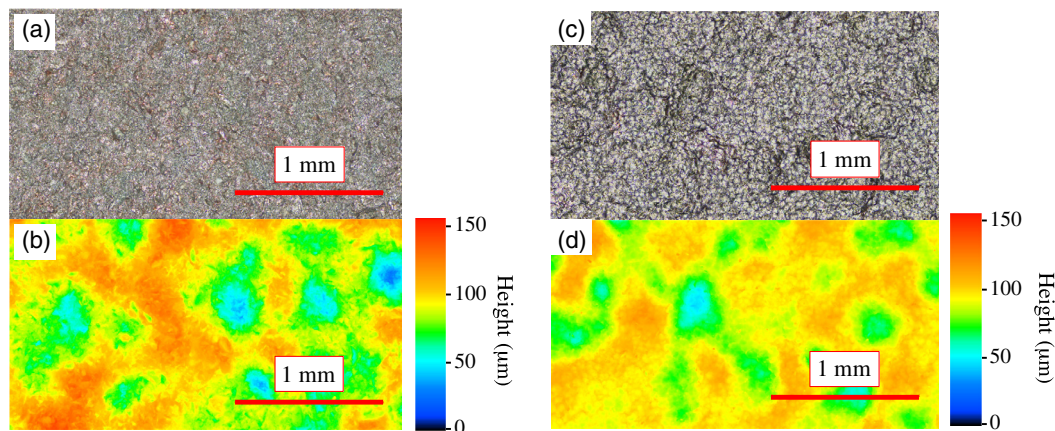


Fig. 3 (a) Optical micrograph and (b) laser scanning confocal height map, showing the sample surface following grit-blast cleaning of the surface. (c) Bead blasted optical micrograph and (d) height map show minor signs of bead indentations, which modulates the surface at length scale of ~ 100 μm .

angle of incidence may vary, and we can expect a variation in the absorptivity for both S- and P-polarized light. For example, from the height maps of Figs. 3(b) and 3(d), we can estimate that the local angle of incidence can vary by as much as 20 to 30 deg. Also, the surface roughness will increase the absorptivity due to multiple scattering effects and absorption via defects. It is important to consider these complicating factors when assessing absorptivity of laser-processed steel surfaces under practical conditions.

3.2 Thermal Model and Numerical Analysis

A commercial code (FlexPDE, Spokane Valley, Washington) was used to model the interaction of the diode light with the HY-80 steel plate. This finite-element-based code solves the three-dimensional nonlinear heat transport equation subject to arbitrary boundary and initial conditions. The simulations were performed over a domain corresponding to the full part used in the experiment ($6.35 \times 152.4 \times 152.4 \text{ mm}^3$). A nonuniform, adaptive mesh of $\sim 70,000$ elements was used, which tracked the laser spot. The code features adaptive time step control as well as adaptive meshing so that regions with large temperature gradients may be adequately resolved. For these calculations, we used natural convection boundary conditions (film heat transfer coefficient of $10 \text{ W/m}^2\text{-}^\circ\text{C}$) as well as a radiative (T^4) boundary condition on the illuminated surface based on an emissivity function $\varepsilon = 0.083 + 9.7 \times 10^{-5} \bullet T$, where T is in Kelvin.²³

In addition to the geometry of the slab and the location of the various thermocouples described above, additional inputs to our model include the spatial distribution of the laser diode radiation, the displacement of the laser beam across the sample as a function of time, and the physical properties of the HY-80 material. We note that it is critical to use spatial irradiance profiles specific to a given diode current since they vary with current. Figure 4 shows the irradiance pattern for a laser diode current of 23 amps, corresponding to a laser

beam power of $\sim 350 \text{ W}$ measured by a coherent thermopile power sensor. The irradiance profile at higher powers is similar to the one shown, with the major difference being an increase in the slow-axis divergence of the beam (vertical). The 2-D irradiance distribution is used as a table look-up in our finite-element code.

It is important to use temperature-dependent properties for HY-80 as the temperature excursions were expected to be quite large. Unfortunately, only data at room temperature seems to be available for HY-80. We therefore adopted the approach wherein the temperature dependences of the thermal properties of HY-80 were those of the steel HY-130²⁴ but adjusted to give the correct room temperature values.²⁵ The validity of this approach is borne out by the good agreement between the measured and calculated values over a wide range of temperatures. A plot of the thermal properties of HY-80 obtained is shown in Fig. 5. For the thermal conductivity and density curves, polynomial fits were used. For the specific heat data, we did not find a good polynomial fit; instead, we used a look-up table as input to our finite-element code.

Finally, the laser energy coupling determines the heat source for the heat transport equation and is determined by the optical absorptivity. As discussed above, the absorptivity can vary (0.6 to 1) due to the presence of an oxide layer as well as surface roughness. Therefore, we include in our model an adjustable value for absorptivity, α , to give the best match to the thermocouple data. This adjustment is done using the method of least squares with the peak temperatures used as the minimization criteria. That is, we minimize the function $f(\alpha)$ given by

$$f(\alpha) = \sum_{m=1}^n [T_{\text{max,calc}}^m(\alpha) - T_{\text{max,meas}}^m]^2, \quad (1)$$

where n is the number of thermocouples and T_{max}^m is the maximum temperature of thermocouple m . For these

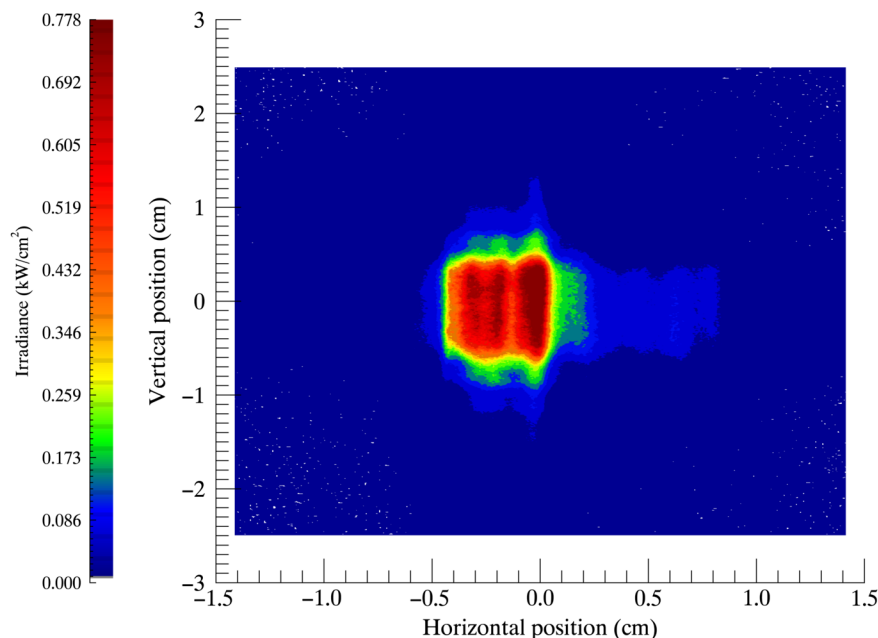


Fig. 4 Laser diode irradiance measured at the sample surface for an operating current of 23 amps ($P = 312 \text{ W}$).

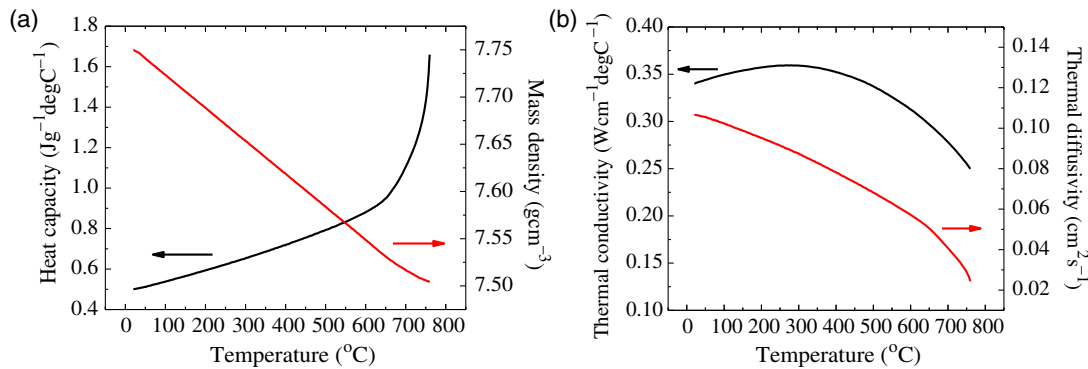


Fig. 5 Heat capacity (a) and thermal conductivity (b) of HY-80 steel (Ref. 24).

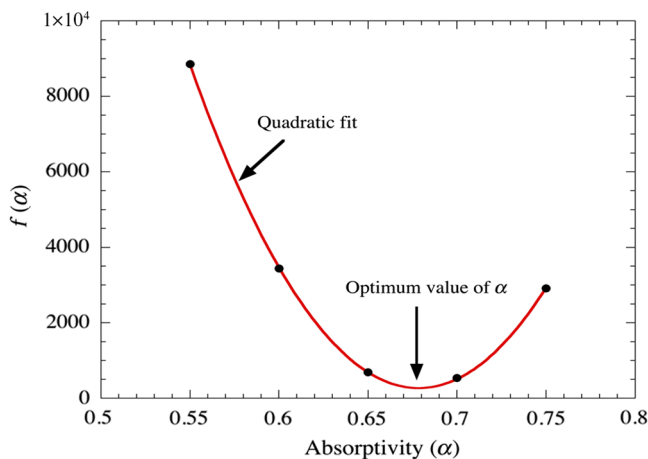


Fig. 6 Plot of the minimization function for determining the optimum value of absorptivity. See Eq. (1).

calculations, α is independent of time and temperature. For all cases, a minimum of five model calculations were performed in order to sufficiently resolve the minimum in $f(\alpha)$. As an example, the function $f(\alpha)$ so obtained is shown in Fig. 6. In this case, the optimum value of absorptivity is 0.68, which is higher than the value of 0.63 calculated for wrought material shown in Fig. 2, as expected.

In evaluating Eq. (1), there are experimental and computational uncertainties. The error of thermocouple measurements is about 3%. Taking into account the computational accuracy, a very conservative value for the total uncertainty is that $\Delta y \sim 0.1 y_{\max}$. If we then do a nonlinear least squares calculation using these uncertainties as weights, then the parameter standard error is about 8% of the parameter's value. Thus, the uncertainty in the optimum value of absorptivity is $\sim 8\%$ as well.

4 Results and Discussion

4.1 Bulk Temperature Measurements and Extracted Surface Absorptivity Values

A set of experiments with several laser powers, designated by their corresponding diode currents (23, 25, 27 amps), were performed on both grit-blasted and bead-blasted surfaces. In each case, thermocouple data were collected from at least four positions, along with thermal camera data. The maximum thermocouple values were then analyzed using

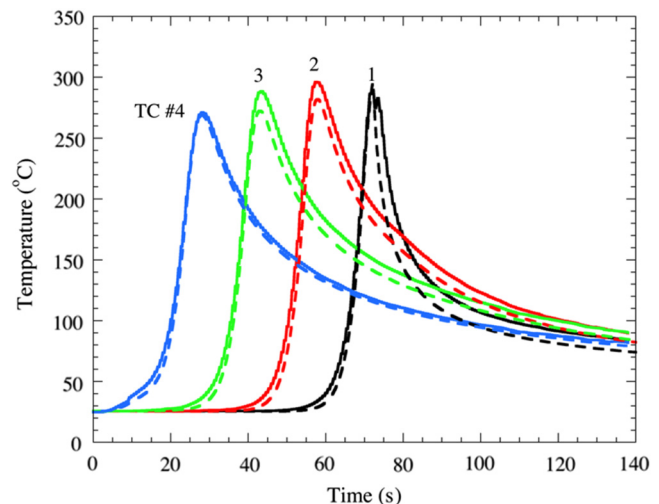


Fig. 7 Comparison of measured thermocouple temperatures (solid lines) and simulated temperatures (dashed lines) for the case of a bead-blasted sample irradiated with 483 W of P-polarized laser light. A constant (in time and temperature) absorptivity of 0.661 was used for the simulated curves.

Eq. (1) to find the best fit absorptivity values for each dataset. A comparison between measured and calculated thermocouple temperatures (using the best fit absorptivity) for a bead-blasted plate exposed to a 483-W incident P-polarized laser beam (25 amps) is shown in Fig. 7. The simulations of Fig. 7 corresponded to an absorptivity of 0.661. In an attempt to resolve the variation of temperature in depth and include a spread of peak temperatures to calibration, the model, the four thermocouples readings, shown in Fig. 7, varied in depth (mm): TC1(3.18), TC2(3.81), TC3(4.45), and TC4(5.08). The agreement between measured and calculated curves is quite good over the time span shown even though only the peak temperature was used to derive the optimal absorptivity values. Note also the variation in the temporal histories as well as the initial delay is well-captured by the model. Some deviation in the calculated/experimental thermal histories is observed at long times, where the effect of thermal boundary conditions such as convection and radiation could be important. Changes in surface emissivity due to oxidation through laser processing may also play a role, as discussed below. Table 1 summarizes the extracted absorptivity using the finite-element simulations.

Table 1 Summary of experimental conditions and extracted HY-80 absorptivity using model fits to thermocouple data. Peak surface temperatures obtained using extracted values are also shown for the P-polarized, bead-blasted case as an example. Data for S-polarized exposures at 353 W were excluded due to poor surface quality.

Current (A)	P (W)	$T_{P, BB}$ (°C)	α , P-polarized		α , S-polarized	
			Grit	Bead	Grit	Bead
23	353	402	0.629	0.673	—	—
25	483	526	0.744	0.661	0.622	0.753
27	612	881	0.813	0.828	0.73	0.685

All cases were included except the lowest power (383 W) of the S-polarized data, where surface flaws are believed to have caused a large variation in surface heating. A minimum value of $\alpha = 0.622$ was observed for the S-polarized grit blasted sample at $P = 483$ W, whereas a maximum of $\alpha = 0.828$ was observed for the P-polarized, bead-blasted samples. For both polarizations, there is an observed increase in absorptivity of the grit-blasted samples with increasing laser power. While an increase of absorptivity with temperature is consistent with the known $\sim 2 \times 10^{-5}/K$ temperature dependence of absorptivity of common metals,²⁶ the magnitude of the increase ($\sim 3 \times 10^{-4}/K$) points toward additional contributions, likely oxidation. We note that the oxidation likely caused during processing could also lead to changes in emissivity thus causing a change in radiative heat loss, which will affect the cooling rates, as shown in Fig. 7.

For the bead-blasted case, the trend with laser power and material temperature is not so clear, with a slight decrease in α for P-polarized light with increasing power from 353 to 483 W. Similarly, a small decrease in α for S-polarized light with increasing power is observed from 483 to 612 W. Because the bead blast treatment was more aggressive and produced noticeable indentations in contrast to the grit blasting, variations in local surface morphology may contribute to variations in the extracted absorptivity for this surface preparation. For all except the 483-W bead-

blasted case, an increase in absorptivity is observed in changing from S- to P-polarization as expected from the predicted optical properties, as shown in Fig. 2. Generally, all absorptivity values extracted fell in the range between that predicted for unoxidized, wrought Fe (~ 0.6), and iron oxide (~ 1). Interestingly, the highest absorptivity values were extracted for the highest powers, which may indicate more prevalent oxidation levels at higher temperatures. By comparing the P-polarized α values at 483 W with the S-polarized values at 612 W, we found a performance “gain” for both grit- and bead-blasted surfaces. That is, for the roughened sample surfaces used here, rotating polarization from S- to P-polarization has approximately the same effect as increasing the laser power by $\sim 25\%$ on average.

4.2 Surface Temperature Distribution and Comparison with FSW Length Scales

With the model validated through the preceding analysis, we now turn to examining the predicted surface temperature profiles. In general, the thermal conductivity of structural carbon steels tends to be low (0.1 to 0.4 $W\ cm^{-1}\cdot^{\circ}C^{-1}$) compared to pure metals and most metal alloys,²⁷ such that the HAZ extends very little beyond the illuminated region. This limited heat penetration is very evident in Fig. 8(a), which shows a contour plot of the temperature field on the incident surface at the end of a 25 amp (483 W) scanned exposure.

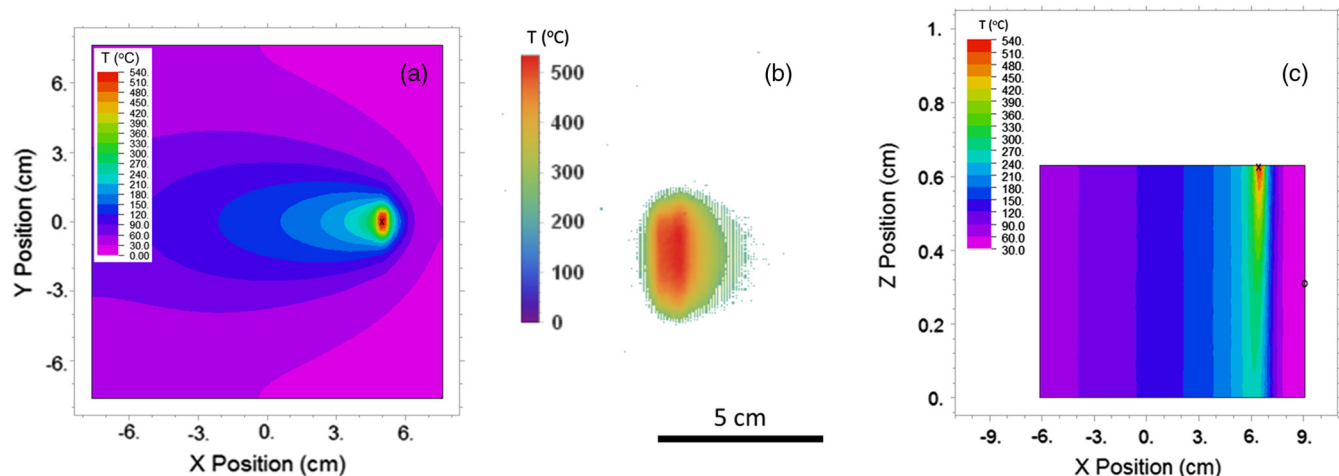


Fig. 8 (a) Calculated surface temperature (°C) at end of laser beam traversal for the 25 amp, 483 W case. (b) The corresponding thermal camera image highlights the highly confined peak temperature zone described in the text. (c) Same simulations as in (a), but showing the temperature distribution through thickness of slab.

As shown in Fig. 8(a), a peak temperature zone in the range $500 < T < 529^{\circ}\text{C}$ is well contained within a region of $\sim 0.5 \times 1 \text{ cm}^2$, with temperatures falling off steeply to $\sim 200^{\circ}\text{C}$ over 1 to 2 cm. The localized simulated temperature field is experimentally confirmed in Fig. 8(b), which shows IR thermal camera data corresponding to the 25 amp simulation of Fig. 8(a). Absolute temperature scale for the thermal camera data in Fig. 8(b) is determined by calibrating to the measured thermocouple readings under the laser heated spot and assuming constant emissivity. Because of the limited heat transport away from the laser irradiated area, the shape of the laser diode irradiation pattern (see Fig. 4) can be observed. This lack of thermal spreading also implies that beam shaping may be a useful tool to precisely control the heat and temperature distributions to maximize the utility of laser pre- or postheating for FSW. We can also examine the temperature distribution in the bulk using simulation code, and compare it with the measured HAZ in Sec. 4.3. As shown in Fig. 8(c), the peak temperature zone of 500°C to 529°C extends $\sim 500 \mu\text{m}$ below the surface, with the temperature decreasing to $\sim 300^{\circ}\text{C}$ at the rear surface. The significant heating on the rear surface highlights the caution that must be exercised when interpreting these results. Typical FSW conditions involve an anvil or substrate, which provides different thermal boundary conditions. In particular, the addition of another thermal pathway, such as an anvil, increases the amount of diode power required to reach a given surface temperature.

The localization of heating will influence an actual LAFSW application. For example, Fig. 9 shows the maximum temperature (T1) on the surface and the temperature 1 in. (25.4 mm) downstream (T2) where, hypothetically, a FSW tool would be located. As can be seen, a significant temperature gradient exists between T1 and T2. Thus, if a higher temperature at the location of the tool were required, either more diode power would be required (which may raise the maximum temperature to an undesirable value) or the distance between the tool and laser exposure would need to decrease.

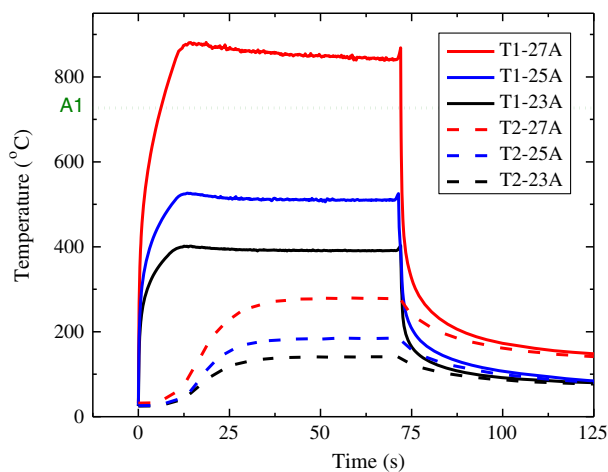


Fig. 9 Calculated surface temperature histories for P-polarized, bead-blasted conditions at point of maximum temperature (T1, solid curves) and at location of hypothetical tool (T2, dashed curves). Note that because of the poor thermal conductivity, a significant temperature gradient exists over the 1 in. spacing. The austenitic phase transition temperature, A1, is indicated by the dotted line.

4.3 Microstructure Characterization of the Heat-Affected Zone

Macroscopic changes in surface appearance could be observed by inspection of plates under varying experimental conditions. Optical micrograph analysis of HY-80 laser-heated plates further revealed an increased HAZ with increasing laser power. At 25 amps (353 W) and below, there was no visible HAZ within the bulk. The increase in the visible “lateral” HAZ is directly due to the increased laser power. Change in polarization from S to P also causes an increased lateral HAZ, which can be seen by comparing the top and bottom passes of the inset of Fig. 1, although this change was small, so additional methods were used to verify this result. Change in surface preparation from bead blasting to grit blasting, which results in a reduction in surface polish leading to an expected increase in laser absorptivity for a given laser current and polarization, caused an increased planar HAZ (not shown), although this change is also difficult to assess using macrographs alone. Although lateral macrograph analysis of laser heated sections is qualitative, the results are easily attainable and consistent with more refined methods conducted in this research.

Optical micrographs of etched cross-sections obtained from a laser heat treatment at 612 W or greater (to be reported in a separate publication) under P-polarization conditions clearly show a visible transverse HAZ that extends below the surface of the work piece (Fig. 10). This HAZ is due to the work piece achieving a temperature greater than the allotropic phase transformation from ferrite to austenite (727°C). Since no controlled cooling occurred following laser heating, air cooling alone resulted in the rapid transformation of austenite to martensite leading to increased martensite in the HAZ. Inspection of the transition area between the HAZ and the base metal region clearly shows a change in grain structure with additional fine needle-like martensite grains appearing in the HAZ compared to the base metal. Of the conditions studied here, a visible transverse HAZ only occurs when operating the laser at 612 W with P-polarization (on either surface preparation condition). Under P-polarized conditions below 612 W or at S-polarized conditions of 612 W or less, no such HAZ exists. This microstructural feature helps clearly establish a temperature condition corresponding to 727°C .

Additional characterization was carried out using EDS and EBSD to further probe the polarization- and power-dependent HAZ. EDS results show that although a phase change occurs in the HAZ, there is no compositional change or indication of change in distribution of constitutive elements in the workpiece. EBSD results shown in Fig. 11 are consistent with optical and electron microscope images (Fig. 11), showing a smaller grain size in the HAZ due to the formation of additional martensitic grains after cooling. The crystallographic features of martensite in low carbon steels, such as HY-80, are discussed in detail by other authors,²⁸ and the phase transformations that occur in these steels during laser heating and laser joining have also been discussed.²⁹ The results shown in this research are similar to previous studies in that the laser heating causes a phase transformation from a predominantly ferritic phase (specifically tempered martensite for HY-80) to austenite and then to a new additional martensite phase upon cooling. This is shown by the transformation from comparatively large tempered

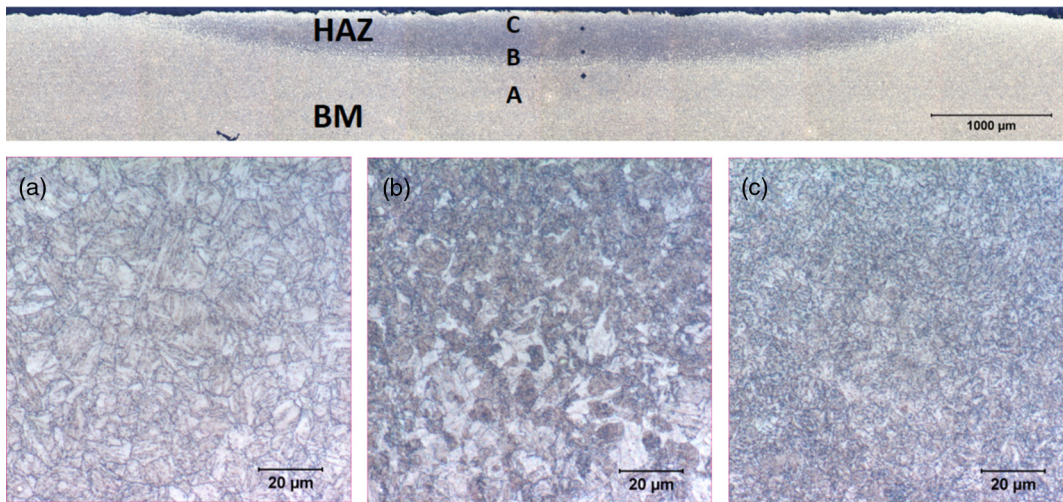


Fig. 10 Optical micrographs of cross sections of samples exposed to 612 W, P-polarized laser exposures with inset areas (a), (b), and (c) showing the transition from tempered martensite in the base metal (BM) to martensite in the HAZ. Of the three laser power conditions studied, this transition only occurred for the 612 W, P-polarized case.

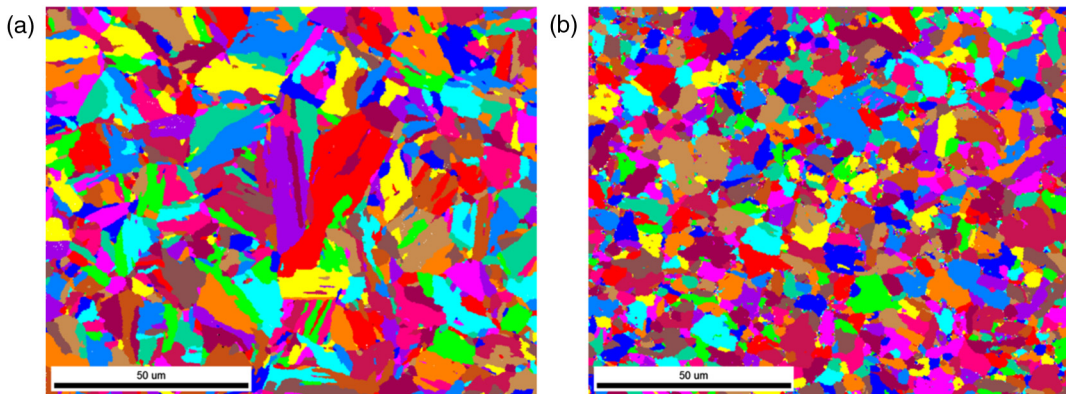


Fig. 11 Unique color grain maps produced by EBSD from (a) base metal and (b) HAZ showing the transformation from tempered martensite to martensite due to laser heating. In both (a) and (b), the direction of laser scanning is normal to the page.

martensite grains with a high degree of misorientation angles [Fig. 11(a)] to those with comparatively smaller martensitic grains in the HAZ with nominally equiaxed grains, i.e., grains with low misorientation angles [Fig. 11(b)] following laser heating. A more detailed analysis of grain morphology and resultant material properties may reveal more insights.

5 Conclusions

We have analyzed the temperature rise in HY-80 steel test plates caused by diode laser irradiation at high angle of incidence in two orthogonal polarization states and compared our results to finite-element modeling of laser-induced heating. Roughened surfaces were prepared and experimentally studied to mimic realistic engineered surfaces commonly encountered in FSW and other industrial applications. Using a single fit parameter (optical absorption), we were able to simulate temperature versus time curves measured by embedded thermocouples and predict surface temperature behavior due to laser scanning. Surface temperatures simulated and measured using IR imaging revealed a highly confined heating zone due to the low diffusivity of the steel

plates. Microstructure changes within the HAZ below the surface were evaluated using optical microscopy and EBSD, which indicate the creation of a quenched martensite phase from a high temperature austenite phase. An average of ~25% decrease in absorptivity was observed for S-polarized light compared to P-polarized, consistent with an observed decrease in HAZ, which was less than predicted (~50%) for wrought, unoxidized steel at 60-deg angle of incidence based on the calculated Fresnel reflection coefficients. The presence of an oxide layer (e.g., Fe_3O_4) is presumed to lead to the increased absorptivity extracted from our temperature measurements. The observed reduced polarization sensitivity is also attributed to the surface roughness and defects of the steel plates and multiple scattering effects, which are beyond the scope of this study.

Acknowledgments

The authors are eternally grateful to have received guidance from and worked with the late Dr. W. Howard Lowdermilk, to whom this article is dedicated. This work was funded through a Laboratory Directed Research and Development

grant 15-ERD-037 and performed under the auspices of the U.S. Department of Energy by Lawrence Livermore National Laboratory under contract DE-AC52-07NA27344.

References

1. C. D. Orth, S. A. Payne, and W. F. Krupke, "A diode pumped solid state laser driver for inertial fusion energy," *Nucl. Fusion* **36**, 75–116 (1996).
2. D. J. Richardson, J. Nilsson, and W. A. Clarkson, "High power fiber lasers: current status and future perspectives," *J. Opt. Soc. Am. B* **27**, B63–B92 (2010).
3. Y. F. Chen et al., "Optimization in scaling fiber-coupled laser-diode end-pumped lasers to higher power: influence of thermal effect," *IEEE J. Quantum Electron.* **33**, 1424–1429 (1997).
4. R. J. Beach et al., "End-pumped continuous-wave alkali vapor lasers: experiment, model, and power scaling," *J. Opt. Soc. Am. B* **21**, 2151–2163 (2004).
5. M. J. Matthews et al., "Micro-shaping, polishing, and damage repair of fused silica surfaces using focused infrared laser beams," *Adv. Eng. Mater.* **17**, 247–252 (2015).
6. M. von Allmen and A. Blatter, *Laser-Beam Interactions with Materials*, Springer-Verlag, Heidelberg (1998).
7. J. P. Kruth et al., "Consolidation phenomena in laser and powder-bed based layered manufacturing," *CIRP Ann.* **56**, 730–759 (2007).
8. A. Temmler, E. Willenborg, and K. Wissenbach, "Laser polishing," *Proc. SPIE* **8243**, 82430W (2012).
9. B. Baker et al., "Use of high-power diode laser arrays for pre- and post-weld heating during friction stir welding of steels," in *Friction Stir Welding and Processing VIII*, R. S. Mishra et al., Eds., pp. 21–36, John Wiley & Sons, Inc., New York (2015).
10. G. Kohn et al., "Laser-assisted friction stir welding," *Weld. J.* **81**, 46–48 (2002).
11. S. L. Campanelli et al., "Analysis and comparison of friction stir welding and laser assisted friction stir welding of aluminum alloy," *Materials* **6**, 5923–5941 (2013).
12. G. Casalino et al., "Study of a fiber laser assisted friction stir welding process," *Proc. SPIE* **8239**, 823913 (2012).
13. G. Casalino et al., "Laser-assisted friction stir welding of aluminum alloy lap joints: microstructural and microhardness characterizations," *Proc. SPIE* **8963**, 896316 (2014).
14. W.-S. Chang et al., "Microstructure and mechanical properties of hybrid laser-friction stir welding between AA6061-T6 Al Alloy and AZ31 Mg alloy," *J. Mater. Sci. Technol.* **27**, 199–204 (2011).
15. N. Able and F. Pfefferkorn, and ASME, "Laser-assisted friction stir lap welding of aluminum," in *Proc. ASME* (2005).
16. K. H. Song, T. Tsumura, and K. Nakata, "Development of microstructure and mechanical properties in laser-FSW hybrid welded Inconel 600," *Mater. Trans.* **50**, 1832–1837 (2009).
17. Y. F. Sun et al., "Microstructure and mechanical properties of S45C steel prepared by laser-assisted friction stir welding," *Mater. Des.* **47**, 842–849 (2013).
18. Y. F. Sun et al., "Spot friction stir welding of low carbon steel plates preheated by high frequency induction," *Mater. Des.* **54**, 450–457 (2014).
19. S. Elhadj, M. J. Matthews, and S. T. Yang, "Combined infrared thermal imaging and laser heating for the study of materials thermophysical and processing properties at high temperatures," *Crit. Rev. Solid State Mater. Sci.* **39**, 175–196 (2014).
20. P. B. Johnson and R. W. Christy, "Optical-constants of transition-metals—Ti, V, Cr, Mn, Fe, Co, Ni, and Pd," *Phys. Rev. B* **9**, 5056–5070 (1974).
21. V. Goossens et al., "Optical properties of thin iron oxide films on steel," *Surf. Interface Anal.* **38**, 489–493 (2006).
22. D. Bergstrom, J. Powell, and A. F. H. Kaplan, "The absorption of light by rough metal surfaces—a three-dimensional ray-tracing analysis," *J. Appl. Phys.* **103**, 103515 (2008).
23. B. Karlsson and C. G. Ribbing, "Optical-constants and spectral selectivity of stainless-steel and its oxides," *J. Appl. Phys.* **53**, 6340–6346 (1982).
24. V. Papazoglou, "Analytical technique for determining temperatures, thermal strains and residual stresses during welding," PhD Thesis, p. 292, Department of Ocean Engineering, Massachusetts Institute of Technology, Cambridge, Massachusetts (1981).
25. T. J. Holmquist, *Strength and Fracture Characteristics of HY-80, HY-100, and HY-130 Steels Subjected to Various Strains, Strain Rates, Temperatures, and Pressures*, Final report, Honeywell Inc., Brooklyn Park, Minnesota (1987).
26. S. Boyden and Y. Zhang, "Temperature and wavelength-dependent spectral absorptivities of metallic materials in the infrared," *J. Thermophys. Heat Transfer* **20**, 9–15 (2006).
27. F. Cervera, *Thermal Properties of Metals*, ASM International, Materials Park, Ohio (2002).
28. H. Kitahara et al., "Crystallographic features of lath martensite in low-carbon steel," *Acta Mater.* **54**, 1279–1288 (2006).
29. K. H. Lo, F. T. Cheng, and H. C. Man, "Laser transformation hardening of AISI 440C martensitic stainless steel for higher cavitation erosion resistance," *Surf. Coat. Technol.* **173**, 96–104 (2003).

Sheldon S. Q. Wu received his doctorate degree in electrical engineering with a focus in photonics from University of California at San Diego in 2009. Since then, he has worked as a laser physicist at Lawrence Livermore National Laboratory in Livermore, California. He has made technical contributions in the fields of diode-pumped alkali lasers, precision Compton scattering light sources for nuclear photonics applications, and coherent diode laser sources. His primary scientific interests include laser physics, laser-matter interactions, classical and quantum electrodynamics, high field physics, and quantum optics.

Bradford W. Baker has served as a submarine officer in the US Navy for over 20 years and is now a permanent military professor at the US Naval Academy teaching mechanical and nuclear engineering. His research interests include nuclear materials, additive manufacturing, and material processing methods. <http://www.usna.edu/MechEngDept/faculty/baker.php>

Alexander M. Rubenchik received his PhD in theoretical physics from Institute of Nuclear Physics, Novosibirsk in 1974 and the Dr.Sci. degree from Space Research Institute, Moscow, in 1983. Since 1992, he is a physicist at Lawrence Livermore National Laboratory. His works include study of ultrashort laser pulse damage and material processing, fundamental understanding of processes responsible for NIF optics damage and interaction of powerful laser radiation with targets. His main scientific interests are in physics of laser-matter interaction, nonlinear optics, optical damage, laser and plasma physics.

Manyalibo J. Matthews holds a PhD in physics from MIT and a BS degree in applied physics from UC Davis. His research interests include applications in laser-assisted material processing, optical damage, vibrational spectroscopy, and *in situ* characterization of advanced manufacturing processes. Prior to LLNL, he was a member of technical staff at Bell Labs in Murray Hill, New Jersey, and worked on spectroscopic characterization of optical materials. He is a fellow of the Optical Society of America.

Biographies for the other authors are not available.